Design and Analysis of Accelerometer for Range of Motion Applications

1st Ashutosh Sharma
268193

1st Nabeel Ahmad
Khan Jadoon
269143

1st Vaigunthan Puvanenthiram
268198

Abstract—This report introduces a differential capacitance accelerometer principle and the implementation of a reference design, modification of design to meet the design specifications defined for the Range of Motion (ROM) analysis application. The modified design is analysed for its structural and operational stability and evaluated against the design specification and standard design criteria. With the proposed model the sensitivity of 4.62 fF/g was achieved and around 15 mV/g of sense voltage.

1. INTRODUCTION OF DEVICE AND NEED

Accelerometer, as a MEMS device is a critical sensor in consumer products like smartphones, activity trackers and automotive applications. We are targeting this this device for activity monitoring specifically range of motion for rehabilitation purposes. Here is why there's a need for this device:

Progressively increasing the range of motion (ROM) during rehabilitation is crucial to prevent muscle and joint stiffness maintains or restores flexibility, and helps prevent the formation of scar tissue. Monitoring range of motion (ROM) during rehabilitation can be challenging due to human error, inconsistency, and limited real-time data. Smart sensors could offer access to accurate and objective ROM measurements. They could track progress consistently, identify deviations, and alert therapists to potential issues and open the chance for remote monitoring, progress tracking and providing real-time, data-driven insights to guide and personalize the rehabilitation process.

Using an accelerometer to detect and measure the motion of the human body is one of its applications. Here, we design a surface-machined accelerometer for the measurement of the range of motion application for our rehabilitation device. The measurement range is from -4g to +4g which should have a minimum bandwidth of 4 kHz for the general operation range. The accelerometer is of differential capacitance type and it is chosen based on the benefits in sensitivity, temperature stability and design flexibility it offers.

2. METHODOLOGY

For this study, we followed a standard methodology workflow as presented in Fig 1 starting from our reference design. Moreover, the additional branches in analytical and simulation studies are further mentioned in section 3 onwards based on assumptions and conditions we have considered for this model.
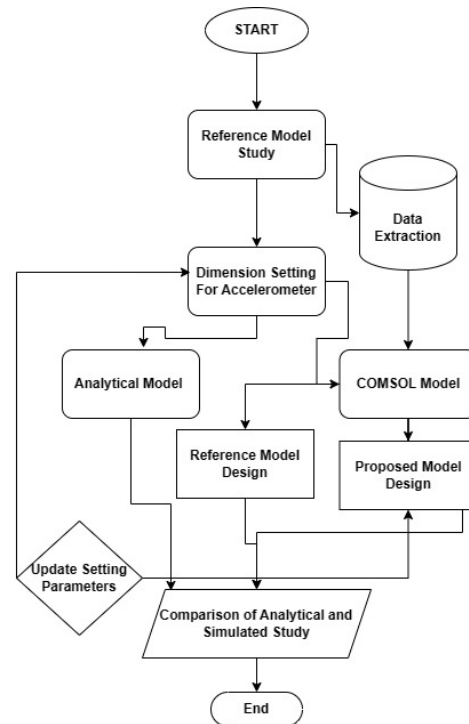

Fig. 1: WorkFlow for this Accelerometer Design

3. PROBLEM DEFINITION FOR ACCELEROMETER

A. Assumptions for Modeling

We have considered the following assumptions for the accelerometer modelling:

- Accelerometer is symmetric around central axis.
- Both structures (up/down) are moving as a unified body.
- Accelerometer doesn't suffer from brittleness or cracks as per selected material.
- Accelerometer is subjected to motion in the lateral axis.
- The cross-sensitivity of the accelerometer in the Y-axis and Z-axis is below 1%.

B. Boundary Conditions

The following Table I presents the boundary conditions for our accelerometer.

Parameter	Specification
Temperature Range	-40°C to 85°C
Acceleration Range	-4g to 4g (tunable up to 16g)
Shock Limit	10,000g
Vibration Limit	2,000g
Mounting Orientation	Lateral
Power Supply Voltage	3.3V to 5V
Frequency Response	10Hz to 1000Hz
Initial Operating Pressure	1 atm

TABLE I: Boundary Conditions for ROM Applications

C. Meshing Conditions

We have optimized the balance between computation power and meshing quality. After trial and error, the following meshing conditions appeared to be suitable for COMSOL modelling as shown in Table II. The curvature factor for our electrode fingers was important as well as for spring dimensions. It was observed that physics-controlled meshing also does the job but our approach to go from "Fine" to "Coarse" where possible was using Triangular meshing resulted in about 1.5 hours reduced from a total of 6 hours.

Parameter	Value
Maximum Element Size	20.8 μm
Minimum Element Size	10 μm
Maximum Growth Rate	1.5
Curvature Factor	0.6
Resolution in Narrow Regions	0.5

TABLE II: Meshing Parameters for Model

4. ACCELEROMETER REFERENCE DESIGN

We have considered a reference study from [1]. In the referenced model, a surface micromachined design of differential capacitance accelerometer for seismic applications ranging from -50g to +50g is proposed. The accelerometer model from the paper is redesigned as shown in Fig 2. The reference design is for a wide acceleration range and the sensitivity it provides in terms of Δx / g is 1.188 nm/g which is very small and there will be challenges in developing a readout circuit.

We have modified the model and tailored it for ROM application from [1]. In the modification, this sensitivity is addressed. In the reference model, the folded beam spring structure used [2] in has a folded beam at the centre with two free beams on either side without any loading. We have replaced it with folded beams connected in series which effectively improved the sensitivity of the accelerometer to 15nm /g for our application.
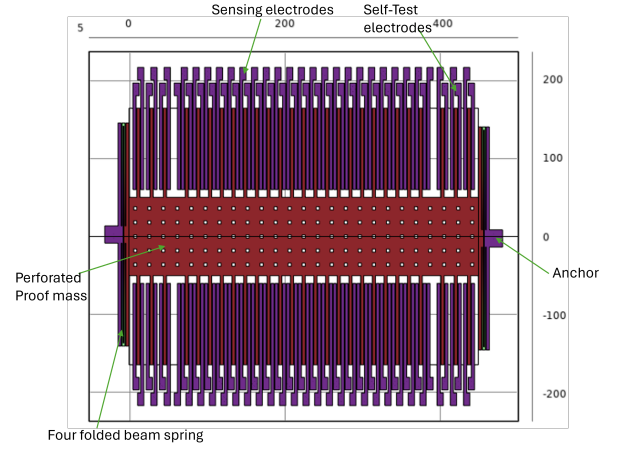

Fig. 2: The differential capacitance accelerometer design illustration from reference paper[1]

5. STUDY OF ACCELEROMETER DESIGN

The accelerometer is designed by keeping the reference design in mind. The differential capacitance is a good solution to enhance the sensitivity.

A. Working principle of differential capacitance accelerometer

The accelerometer design consists of a proof mass which is suspended by the folded beam spring on either side and the fingers attached to the proof mass can move between the electrodes according to the displacement of mass. The finger in between two electrodes is equivalent to two capacitors attached in series with the finger as the common plate. The displacement of the finger creates a capacitance difference between two capacitors and this is proportional to the acceleration.

$$C = \frac{\epsilon A}{d} \tag{1}$$

$$C1 = \frac{\epsilon A}{d + x} \tag{2}$$

$$C2 = \frac{\epsilon A}{d - x} \tag{3}$$

$$\Delta C = \frac{2\epsilon Ax}{d^2 - x^2} \tag{4}$$

$$\Delta C = \frac{2\epsilon Ax}{d^2} \tag{5}$$

where d is the distance between the electrodes, x is the variable displacement, A is the overlap area, and ε is the permittivity of free space. C1 and C2 are the capacitance from the left and right sides of the electrodes. The ΔC in Eqn.4 is non-linear, but considering x $\ll$ d, the Eqn. (4) can be written as in Eqn.5.

The inertial force acts on the system is,

$$F_{inertial} = ma \tag{6}$$

$$F_{damping} = kx \tag{7}$$

$$x = \frac{ma}{k} \tag{8}$$

where, k is the spring constant, m is the mass of the design, and a is the acceleration, with F as Force applied to the

system. From Hooke's law, the relationship between Force act and deflection in spring given by the Eqn. 7, which is the displacement of the proof mass. From Eqn.5 and Eqn.8, the Eqn.9 can be deduced and the differential capacitance directly proportional to acceleration is shown.
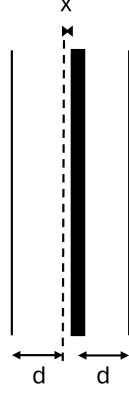

Fig. 3: Illustration of electrodes and finger as differential capacitors

$$\Delta C = \frac{2\epsilon A m a}{k d^2} \quad (9)$$

$$m\frac{d^2 x}{dt^2} + b\frac{dy}{dx} + kx = ma \quad (10)$$

$$\frac{x(s)}{a(s)} = \frac{1}{s^2 + \frac{b}{m}s + \frac{k}{m}} \quad (11)$$

where b is the damping coefficient with other parameters as previously defined. The general spring mass damper model can be considered and the differential equation 10 can be derived and the second order transfer function can be written as 11 [1]. The parameters which can be used to evaluate the accelerometer design are extracted from the governing function and provided in Eqn.12 to 13. The Quality factor (Q) determines the stability of the system based on the type of damping achieved and the resonance frequency (ω_r) provides the bandwidth.

$$Q = \frac{\sqrt{mk}}{b} = \frac{m\omega_r}{b} \quad (12)$$

$$\omega_r = \sqrt{\frac{k}{m}} \quad (13)$$

B. Analytical Calculations

The spring constant of the guided beam structure determines the displacement magnitude of the proof mass and factor to design the accelerometer's sensitivity as required. The reference model's [1] sensitivity is not adequate for our application and thus the spring beam design to folded beams connected in series. The spring structure of the accelerometer is a closed guided beam structure as given in Fig.4a. The spring constant

TABLE III: Parameter Values and Remarks

No	Parameters	Value	Remark
1	Proof of mass Length	448μm	suspended mass
2	Proof of mass Width	200μm	suspended mass
3	No of Sensing fingers	42	-
4	No of Driving fingers	12	-
5	Length of fingers	140μm	electrode connected with mass
6	Width of fingers	4μm	electrode connected with mass
7	Number of perforations	150	perforation 110μm on proof mass
8	Width of hole (square)	4μm	perforation hole dimension
9	Thickness of Proof mass	2μm	surface polysilicon thickness
10	Beam Length (folded)	420μm	Ref-design - 380μm
11	Beam Width (folded)	2μm	Ref-design - 2μm
12	Capacitance gap	1μm	The gap for displacement
13	Spring beam Length	420μm	Total length of beam
14	Spring beam Width	2μm	Width of beam

of the beam structure is given by Eqn.14; where E is the Young's modulus, L_1, L_2 is the length of a guided beam, H is the thickness along the axis of deflection and W is the width of the beam. The one-half of the beam spring structure is given in Fig.5 and it shows how three folded beams join together to form the complete beam structure. The two folded beams are similar and the third one connected to the proof mass has different L since part of it is connected together with the proof mass. These three folded beams are in series as the force applied is the same and this spring set is in a parallel configuration to the folded beam structure on the other side of the proof of mass.

$$k = \frac{(\pi^4/6)Ewh^3}{(2L_1)^3 + (2L_2)^3} \quad (14)$$
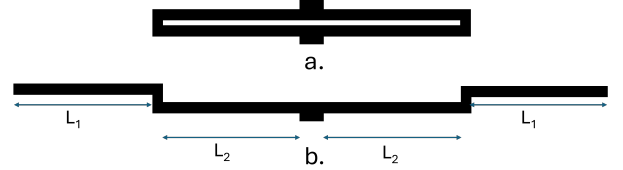

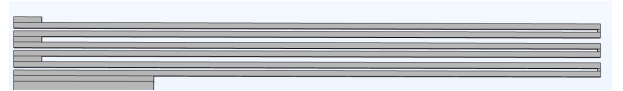Fig. 4: Folded beam structure and equivalent unfolded beam[3]

Fig. 5: Schematic of spring structure of the accelerometer, the symmetrical half portion of the compound folded beam structure provided for clear view

Table.IV shows the dimensions used for the calculation of the spring constant. The effective spring constant of one side compound folded beam is given by the Eqn.15 where the k_1 denotes the spring constant of middle and folded beam connected with anchor and k_2 denotes the spring constant of folded beam fixed with proof of mass. The total spring constant

TABLE IV: Dimensions of the folded beam structure L_1 and L_2

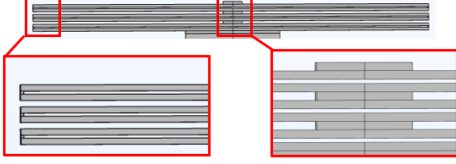| No	Spring Constant	L1	L2
1	k_1	199 μm	199 μm
2	k_2	199 μm	159 μm

Fig. 6: Redesigned Folded Spring Structure

of beam structure is given by k_T in Eqn.16 and the analytical value of k by substituting the values is 0.2546476 N/m.

$$k = \frac{k_1 k_2}{k_1 + 2k_2} \quad (15)$$

$$k_T = 2k \quad (16)$$

The change in capacitance against acceleration is the measure of sensitivity and the proportional voltage change which is used to sense and quantify the acceleration. Eqn.4, is used to calculate the ΔC per g unit of acceleration. The $\Delta C/g$ is calculated as 4.62×10^{-15} F/g.

The damping coefficient (b) is from simulation and determined as (1.54×10^{-5}) and the Proof of mass is calculated with the assumption of cuboidal block with extended beams (fingers) and through holes with sqare openings and have constant density. The analytically calculated ω_r and Q together with sensitivity analysis results tabulated in V.

We have modifications from reference design Fig 3 for spring design. These changes are presented in Fig 6.

TABLE V: Summary of Analytically Calculated Parameter Values and Metrics

No	Parameters	Value	Remark
1	Spring constant - K	0.2546476 N/m	-
2	Mass (Movable mass) - M	5.5002×10^{-10} Kg	Per-mass and fingers
3	Resonance frequency - ω_r	21.5 kHz	
4	Slip film - D_{sl}(s	2.93×10^{-6} Ns/m	Damping Coefficient
5	Air Drag - D_{ad}(s	1.92×10^{-8} Ns/m	Damping Coefficient
6	Quality Factor - Q	0.77	-
7	Sensitivity (capacitive)	4.62 fF/g	$\Delta C/g$
8	Sensitivity (displacement)	21.18 nm/g	$\Delta x/g$
9	Sensitivity (sense voltage)	78.2	μV/g (5mV)
10	Brownian Noise	21.46 ng/√Hz	-

6. SENSITIVITY ANALYSIS

A parametric study is done to analyse the displacement of the mass due to acceleration in the range from -4g to +4g. It follows that at an acceleration of 1g, we obtain a maximum mass displacement of 15nm implying that the sensitivity along the x-direction is 15nm/g.
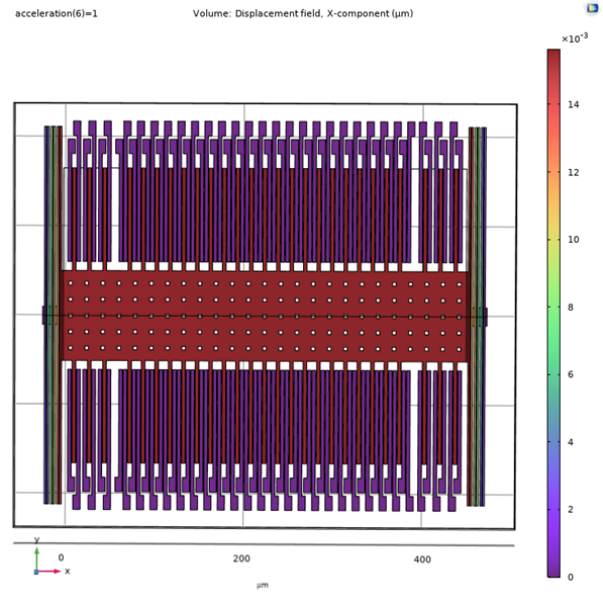

Fig. 7: Sensitivity in X-axis

Hence, with the parametric study of acceleration, a linear graph is obtained between displacement and acceleration along the x-direction.
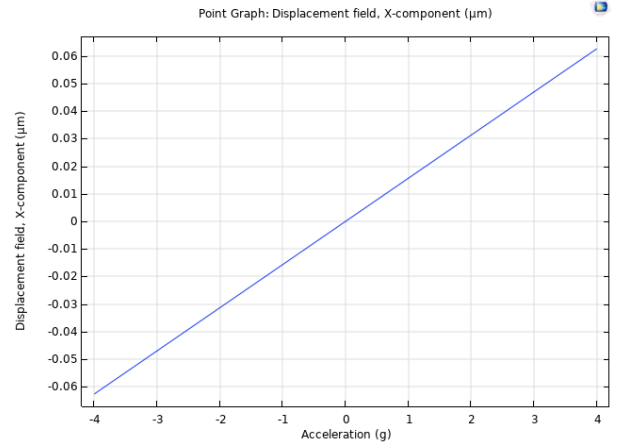

Fig. 8: Displacement vs Acceleration

For this accelerometer, the acceleration range was obtained in non-linear mode as shown in Fig 9 and it has been observed that this can be tuned up to +-16g as can be seen in the model of IMU that was used at Aalto university where as per application it was selected from +-4g to +-16g/ [4].

A. Cross Sensitivity Analysis

The cross-axis sensitivity of accelerometers refers to the extent to which acceleration measured in one axis affects the readings in other orthogonal axes. Various accelerometer designs aim to minimize cross-axis sensitivity to enhance accuracy. The 3-D accelerometers in literature recommended low cross-axis sensitivity of less than 1%, ensuring accurate measurements in each axis [5]. Additionally, the dual-axis fibre
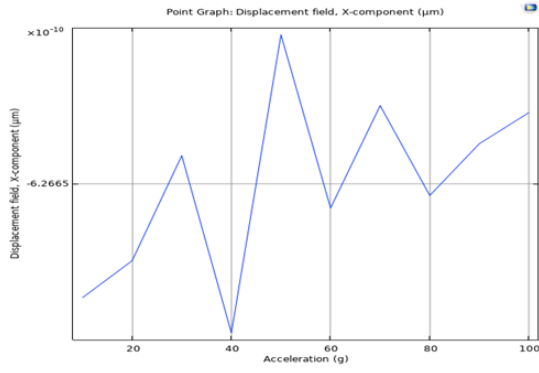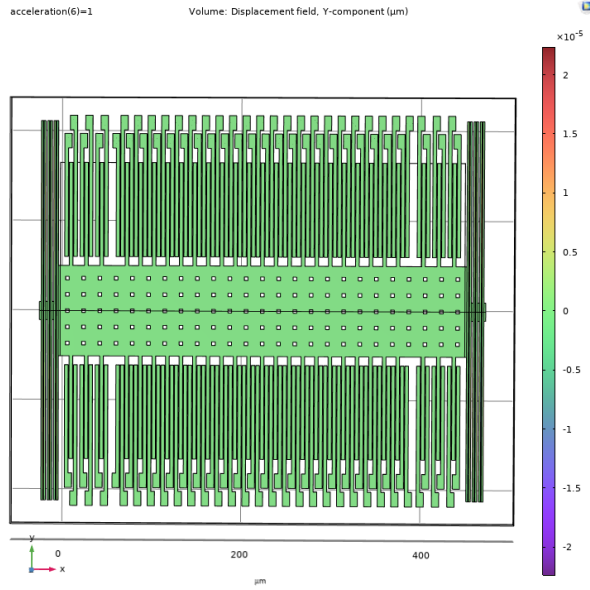
Fig. 9: Non-linear Behavior of Accelerometer

Fig. 10: Cross Sensitivity in Y-axis

Fig. 11: Cross Sensitivity in Z-axis

Fig. 12: Sense Voltage vs Acceleration

optic accelerometer in [6] demonstrates a cross-axis sensitivity below 5.1%, maintaining measurement accuracy in two perpendicular directions. Furthermore, a modified mechanical-optical model addresses cross-axis interference, achieving a significant increase in accuracy when subjected to cross-axis acceleration [7]. These advancements highlight the importance of minimizing cross-axis sensitivity for precise accelerometer measurements in various applications. As per the suggested literature, we aimed to optimize the cross-sensitivity below 1% and results for cross-sensitivity per g are presented in Fig 10 and Fig 11 as compared to actual x-axis sensitivity illustrated in Fig 7. The simulation from COMSOL shows the sensitivity of 15mV/g as shown in Fig 12.

7. EIGEN FREQUENCY ANALYSIS

The operation frequency of the accelerometer needs to be well below the resonance frequency. To meet the criteria, we have performed Eigen Frequency analysis to check the resonating modes in CO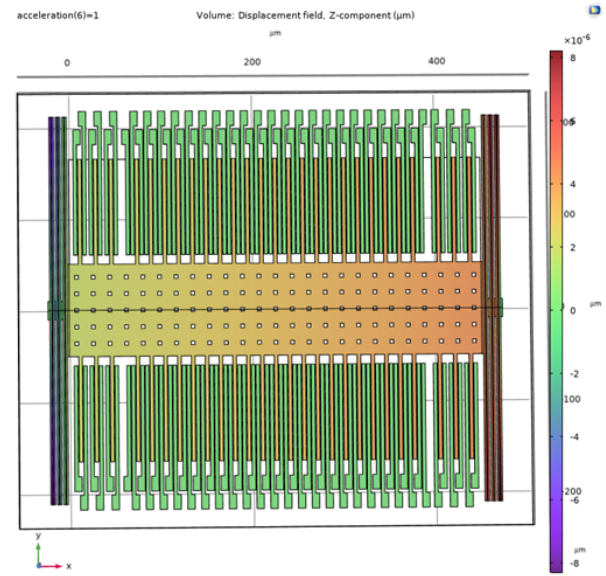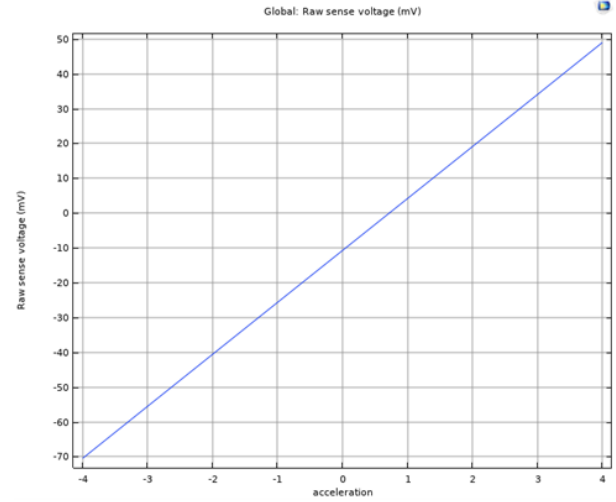MSOL. The model provides eigen-frequency values at various vibration modes, except the first eigenfrequency all other modes of vibration show out-of-plane or torsional vibration as per the simulation results. The lowest Eigenfrequency, which is in the same plane as the intended direction of operation is 4kHz as shown in Fig 13. The resonance frequency at around 4 kHz provides enough bandwidth; considering our range of motion application for patient monitoring. The out-of-plane vibration of the model at 7kHz resonance is provided in Fig.14.

8. STRESS ANALYSIS

The structural integrity of the accelerometer during it's operational range and during edge cases of the application scenarios is critical. The beam springs and joints receives the maximum stress during the operational acceleration range
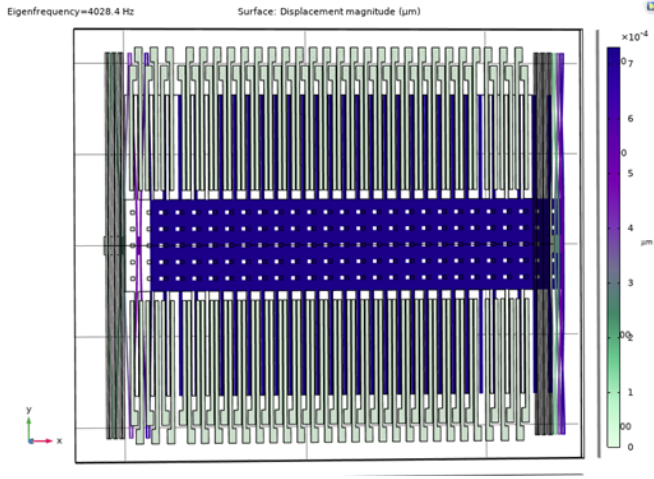
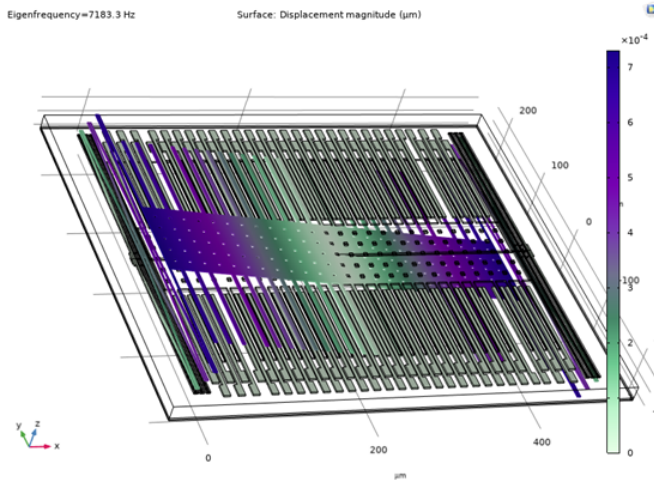Fig. 13: The COMSOL simulation of eigenfrequency of the accelerometer model, at 4K Hz

Fig. 14: The COMSOL simulated 2nd eigen frequency - 7K Hz, which shows the out-of-plane defelection of the structure.
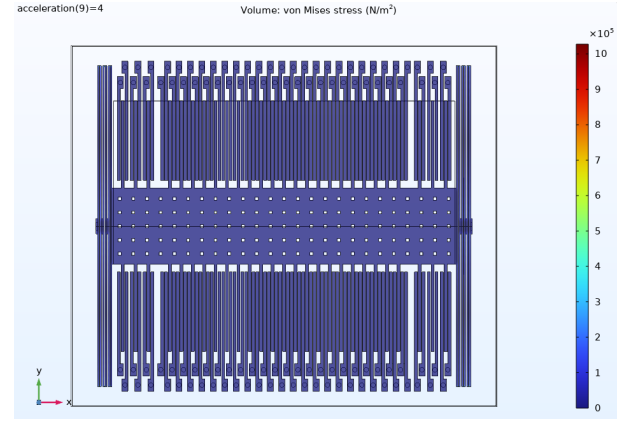

Fig. 15: The stress distribution in accelerometer structure at +4g acceleration, the high stress regions are in the spring structure
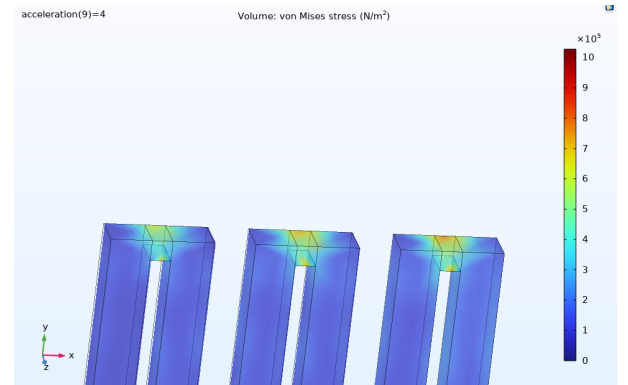

Fig. 16: The enlarged images of spring structure, which shows the high stress regions are at joint sections of the folded beam structure

9. DAMPING ANALYSIS

A. Squeeze Film Damping

The interaction between movable microelectromechanical (MEM) components and the air enveloping them leads to alterations in their dynamic behaviours. These alterations impact various parameters such as resonance frequency, quality factor, and vibration magnitude. The damping effect in the surface machined accelerometer can be modelled considering the effects of squeeze film, slide film and drag force [9]. The squeeze film damping is prominent when the gas film thickness is less than the one-third of width of the vibrational structure; in our case, the perforated mass width is quite larger than the few um gaps [2]. The squeeze film damping is analyzed with COMSOL simulation, and the slide film is calculated based on dimensions and with equations to estimate its effect. As shown in Fig 17, the air film confined between the plate and the adjacent wall experiences compression, inducing an additional pressure within the gap owing to viscous flow dynamics. As the plate separates from the wall, this pressure diminishes. Consequently, the forces acting upon the plate consistently

in the order of 1 MPa and the maximum bearable stress by polycrstalline silicon is demonstrated in [8] as 930 MPa. The Fig.15 shows the stress distribution and Fig.16 shows the zoomed image of it at the +4g acceleration. The maximum stress from the simulation results is 1.03 MPa, which is well below the maximum allowable stress.
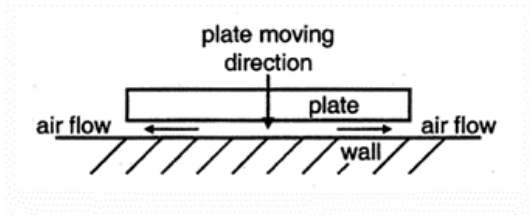
Fig. 17: Illustration of Squeeze Film Damping

oppose its motion. The mechanical work exerted by the plate during its motion is consequently dissipated as heat. In the equation describing this phenomenon, the force (F) is inversely proportional to the velocity (v) of the plate and is represented by the expression F = -cv, where c denotes the coefficient of damping.

In this work, we aim to address squeeze film damping through experimental investigations. Incorporating the volume of surrounding fluid in the analysis is essential, necessitating computationally intensive 3D models. To alleviate computational burdens, a compact and dimensionally reduced model is proposed in COMSOL, enabling the simulation of complex scenarios.

1) Analytical Background: For this model, the generalization is considered for incompressible fluid and modified Reynold's number:

$$\frac{\partial^2 P}{\partial x^2} + \frac{\partial^2 P}{\partial y^2} = \frac{12\mu dh}{h_0 at} \quad (17)$$

And squeeze number is:

$$\sigma = \frac{12\mu u_0 a}{P_L h_0} << 1 \quad (18)$$

The boundary conditions for the linearized Reynolds equation are: Total pressure (P) is equal to a constant value (P_0), expressed as $P = P_0$. The difference between the pressure (P) and the constant value (P_0) is zero, expressed as $P - P_0 = 0$.

2) COMSOL Model Definition for Squeeze Film: For this project, the simulation encompasses 6 distinct geometric configurations derived from experiments detailed in [2]. Utilizing BAO's perforation model, the simulation is implemented within the Thin Film Flow physics interface of COMSOL. Additionally, two extreme scenarios are simulated: one without perforations and another with zero relative pressure at the perforations. The frequency domain formulation is applied, assuming a small amplitude first-order harmonic variation of film pressure, film height, and wall velocity at the frequency of concern. In this model, the boundary conditions entail a vanishing relative pressure (pf = 0) at the perimeter of the proof of mass plate. The relative pressure values in the gas film for the frequency domain analysis are depicted in Fig 18, Fig 19, and Fig 20 for the three respective cases. As anticipated, the pressure magnitude is maximal for the extreme scenario with no etch holes, and minimal for the scenario with zero relative pressure within the etch holes.
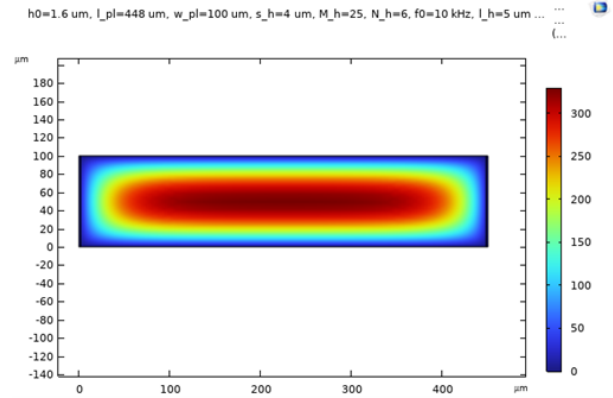

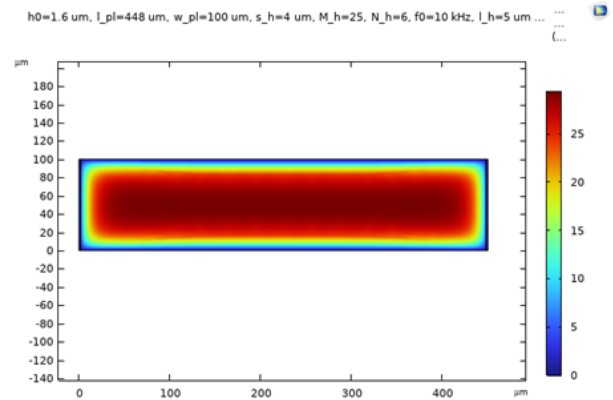Fig. 18: Gas film pressure with no etch holes
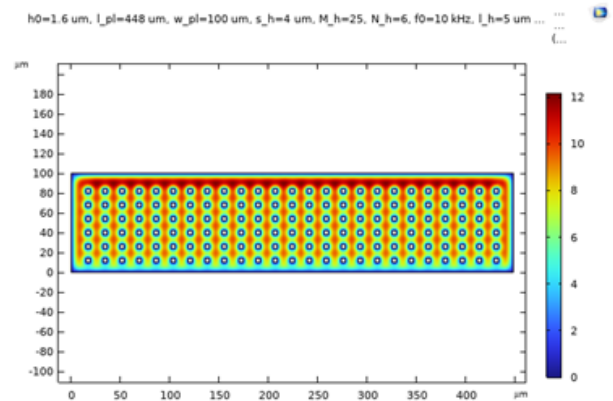

Fig. 19: Gas film pressure with BAO model

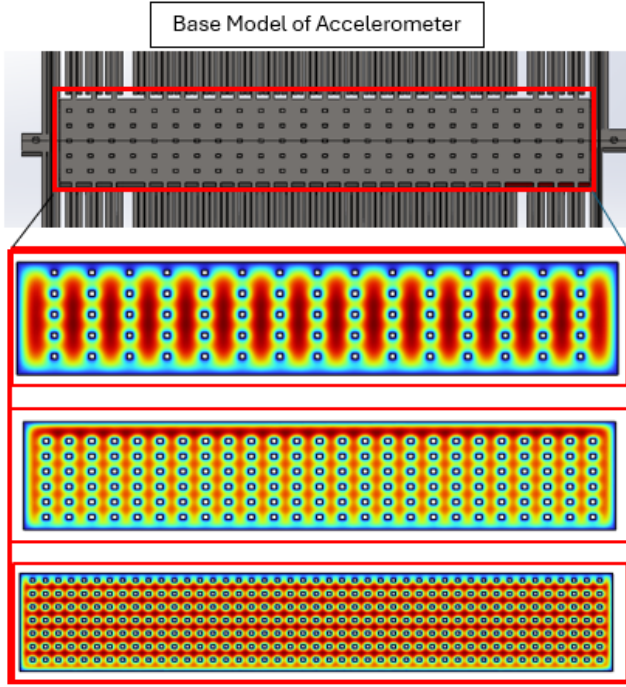Fig. 20: Gas film pressure with zero pressure and perforations

Fig. 21: Comparison of pressure variations at different perforations

Fig. 23: Sweep Parameters for Squeeze Film Damping
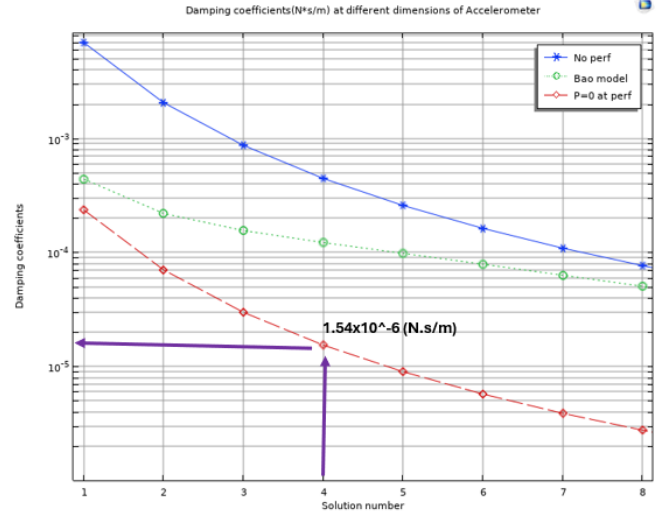
Fig. 24: Final Squeeze Film Damping Coefficient over Height Gap for this Accelerometer
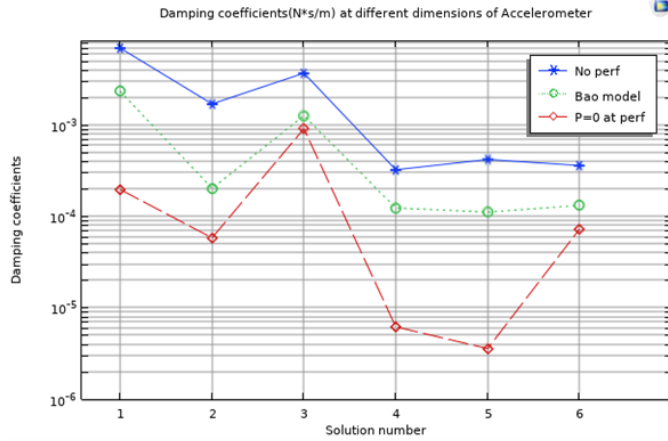

Fig. 22: Damping coefficient for three cases

In the current model, if the perforations decrease or increase, the pressure on the plates keeps increasing. However, the optimal value where the balance between the mass of the plate and perforation scenario is achieved at a number of perforations along length of 25 and along width at 6 as shown in Fig 21.

The damping coefficients for three cases are obtained and shown in Fig 22.

Upon further investigation, we noted that although other parameters like number of perforations, length, width and central frequency do affect the squeeze film damping coefficient not as much as the gap height. Therefore, keeping all the values listed in Fig 23. The parametric sweep over a reasonable gap size from 1-6 μm range is selected and an optimal solution is found at solution 4 with a gap height of 2.5 μm as shown in Fig 24.

B. Slide Film Damping

The device is enclosed by bonding a glass or silicon wafer and thus the top has a gas gap similar to the bottom and the slide film in sidewalls and in fingers is also taken into account. The slide film force is given by Equ.19 and the damping coefficient depends on the effective area (A), gas gap (d) and kinematic viscosity of air (μ).

$$D_{Slide} = \frac{\mu A}{d} \tag{19}$$

$$D_{AirDrag} = \frac{32\mu l}{3} \tag{20}$$

The dimensions and constant values stated in Table.VI is applied to the Equ.19 and the slide film damping is calculated as 2.93×10^{-6} Ns/m. The air drag damping coefficient is given by Eqn.20, where l is the characteristic length which is half of the plate width (perforated mass). The air drag-related damping coefficient is calculated as 1.92×10^{-8} Ns/m

TABLE VI: Dimensions of accelerometer design and physical constants used for Slip film damping coefficient calculation

No	Parameters	Value	Unit
1	Kinematic Viscosity of Air (298 K)	1.8×10^{-5}	Pa s
2	Gas gap - bottom	2	μm
3	Gas gap - top	5	μm
4	Proof mass- Electrode gap	10	μm

10. FREQUENCY RESPONSE AND TIME DOMAIN RESPONSE ANALYSIS

A. Frequency Response

For the accelerometer, from the lumped model we have the equations as follows,

$$m\frac{d^2x}{dt^2} + b\frac{dy}{dx} + kx = F \quad (21)$$

$$\frac{x(s)}{F(s)} = H(s) = \frac{1}{ms^2 + bs + k} \quad (22)$$

From equation 22, we can observe that as the resonance frequency, $\sqrt{\frac{k}{m}}$ decreases, the low-frequency response increases and the high-frequency displacement can be seen as independent of the resonance frequency.

From the calculation, the mass of the design is m = 5.47e-10 Kg. The spring constant value is calculated by solving

$$k = \frac{F}{x} = \frac{ma}{x} \quad (23)$$

where x value arrives from the comsol model for the acceleration of 1g. The spring constant (k) is 3.431e-1 N/m. It can also be seen that the resonant frequency of 3.982 KHz obtained from the k and m values are in congruence with that of the obtained from eigenfrequency simulations.

A rigorous design and analysis is done to find the damping coefficient. The damping coefficient is obtained over a range of values by sweeping the physical dimension parameters over a range as illustrated in Fig 23. By using Matlab code (attached as code 1), iteration is done through a range of b values. It calculates the flatness measure of the magnitude response within the frequency range from 0 to 4000 Hz. The b value that minimizes the flatness measure is considered optimal for achieving a flat response within our frequency range. In this way, we obtain the optimum b value of 1.50e-5 Kg/s as illustrated in Fig 25. Then by simulation in comsol by sweeping the parameters in the proximity range of the desired value of b, the perforation spacing and other related parameters are found. So from the simulation, we obtain the value of b as 1.54e-5 Kg/s for the specific gap height and length parameters as shown in Fig. 24.

Putting these values in equation (22) we draw the magnitude of the transfer function to the frequency to obtain the frequency response as shown in figure 26.

From this, the ζ, damping ratio obtained is 0.5616, the damping coefficient, b as 1.54e-6 Kg/s with the quality factor, Q as 0.8903, signifying that the system is underdamped. This is not too far from the critically damped condition. The
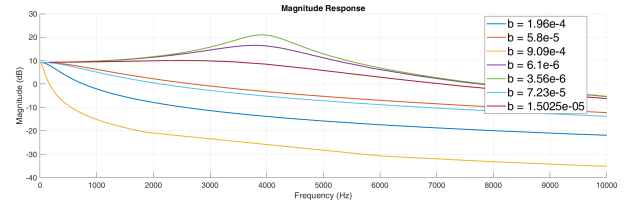

Fig. 25: Frequency Response - Optimum b value calculation
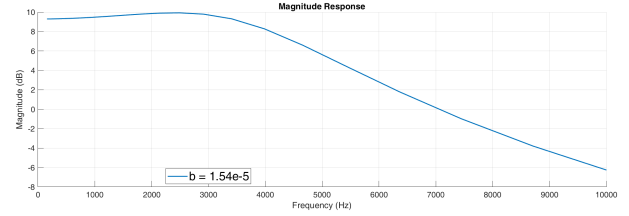

Fig. 26: Frequency response of the accelerometer design

accelerometer should be operated in the low-frequency region, below its mechanical resonant frequency.

B. Time Domain Response

Considering our accelerometer design, a circuit, as shown in Fig 27 is created using the basic circuit elements to simulate the time-domain response. The resistance is b (the damping coefficient), the capacitance is 1/k, k is the spring constant, and the inductance is equal to the mass of our design. At the force of 1g acceleration, we receive the response of position versus time as shown in Fig. 28. Ideally, the response should be a step function, but a physical accelerometer will always have a delay. The most optimum damping coefficient possible from our design is 1.54e-6 N.m/s which will offer optimal speed with a little overshoot or ringing. As discussed previously, the optimum value of the damping coefficient is reached by simulating various dimensions of the perforations from the simulations. As observed in Fig. 28, our system is slightly underdamped, nearer to the critical damping situation with damping coefficient b is 1.54e-6 N.m/s.
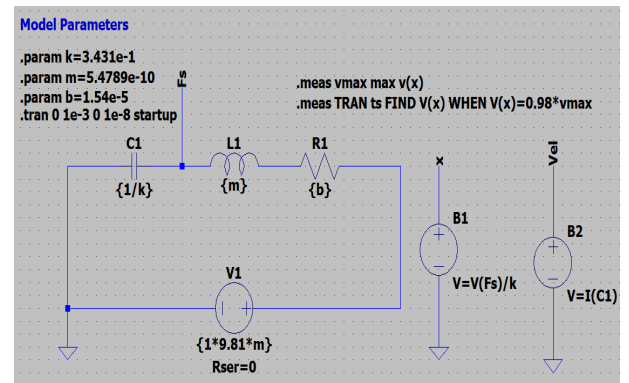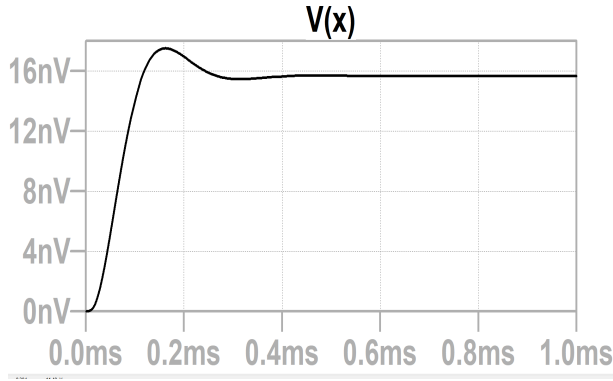

Fig. 27: Lumped Circuit Model

Fig. 28: Position-Time Response

11. NOISE ANALYSIS

In MEMS devices with the measurement of nanometre range motion Brownian noise is significant and it is from the random motion of gas molecules around the proof of mass and between the electrode and finger gaps. The perforated proof of mass has provided significantly more volume for gas molecule distribution and the effect of it in terms of thermal noise generation could be an interesting analysis. Here, using the Eqn.24, where K_B is Boltzmann constant, T is absolute temperature, D is viscous damping coefficient and M is the mass of movable part of accelerometer[10].

$$B_N = \sqrt{\frac{4K_BTb}{m}} \tag{24}$$

The material used for the proof-of-mass can also determine the Brownian noise and in [10], it is suggested that Au has the best results in minimizing the noise. Considering mass production and low-cost accelerometers for consumer electronics it is not an applicable option and regardless the b and m can be optimized to minimize the Brownian noise. Since b is mainly determined by squeeze film damping and the optimization of it affects the m as well an optimized design could be reached while considering other factors like Q and ω_r. The Brownian noise for our model is calculated using Eqn.24 as 21.46 ng/√Hz.

12. DISCUSSION

The differential capacitance accelerometer design presented in this study undergoes a thorough analysis to ensure its suitability for Range of Motion (ROM) monitoring applications in rehabilitation. We achieved a bandwidth of 3KHz and voltage sensitivity of 15mV/g which is sufficient for our target application. Initially derived from a reference model tailored for seismic applications, the accelerometer underwent significant modifications to address sensitivity concerns pertinent to ROM analysis. By replacing the original folded beam spring structure with series-connected folded beams, the accelerometer's sensitivity was enhanced, aligning it with the precise measurement requirements of ROM monitoring.

Theoretical and analytical studies elucidate the accelerometer's working principle, highlighting its sensitivity, resonance frequency, damping coefficient, and quality factor, essential parameters for performance evaluation. Additionally, capacitance sensitivity in the range of fF/g ensures that suitable read-out circuits can be designed in the upcoming semester, thus realizing the rehabilitation monitoring exercises.

A rigorous investigation of squeeze film damping has provided the optimal gap size of 2.5μm on which the response of the system is underdamped with a Q value of 0.89. Initial analysis through changing the geometry of the perforated plate gave us a deep understanding of optimizing the structure of the Accelerometer from a practical point of view.

The summary of achieved specifications as the COMSOL simulation and the generated graph is given in TableVII.

TABLE VII: Summary of achieved Parameter Values from Simulation

No	Parameters	Value
1	Sensitivity	15 mV/g
2	Full-scale Range	-4g to 4g
3	Bandwidth	3000 Hz
4	Sensor Resonance frequency	4028 Hz
5	Self Test Output change	0 - 2 V
6	Quality factor - Q	0.89
7	Damping Ratio - ζ	0.56

13. CONCLUSION

This report presents a design and analysis of a 1-axis capacitive-based comb-drive MEMS accelerometer designed specifically for Range of Motion (ROM) applications. The precise monitoring of muscles is crucial for rehabilitation, as recommended by therapists, necessitating a quick response from the accelerometer. The study demonstrates that viscous damping, influenced by factors such as perforated mass and geometric parameters, plays a significant role in tailoring the system's response to achieve the desired sensitivity and range. Additionally, the optimization of cross-sensitivity ensures consistent system behaviour across a specified frequency range. By optimizing these parameters, the accelerometer can effectively measure and respond to movements within the required range, facilitating enhanced monitoring of muscle motion for rehabilitation purposes.

14. DECLARATION OF CONTRIBUTION

All authors have contributed equally this report starting from the literature study until the final draft. The cross-collaboration among teams ensured a comprehensive understanding of the whole review paper and all sections and flows were approved as a team.

REFERENCES

[1] Ghada Ahmed Khouqeer et al. "Design of MEMS capacitive comb accelerometer with perforated proof mass for seismic applications". In: *Journal of King Saud University - Science* 35.3 (2023), p. 102560. ISSN: 1018-3647. DOI: https://doi.org/10.1016/j.jksus.2023.102560. URL: https://www.sciencedirect.com/science/article/pii/S1018364723000228.

[2] Minhang Bao and Heng Yang. "Squeeze film air damping in MEMS". In: *Sensors and Actuators A: Physical* 136.1 (2007). 25th Anniversary of Sensors and Actuators A: Physical, pp. 3–27. ISSN: 0924-4247. DOI: https://doi.org/10.1016/j.sna.2007.01.008. URL: https://www.sciencedirect.com/science/article/pii/S0924424707000118.

[3] S. D. Senturia. "Microsystem design". In: (2001).

[4] URL: https://docs.arduino.cc/tutorials/nano-33-iot/imu-accelerometer/.

[5] "Development of a High-Precision and Low Cross-Axis Sensitivity 3-D Accelerometer for Low-Frequency Vibration Measurement". In: *IEEE Sensors Journal* (2023). DOI: 10.1109/JSEN.2023.3272578.

[6] "A High-Sensitivity Dual-Axis Accelerometer with Two FP Cavities Assembled on Single Optical Fiber". In: *Sensors* (2022). DOI: 10.3390/s22249614.

[7] "Accurate mechanical-optical theoretical model of cross-axis sensitivity of an interferometric micro-optomechanical accelerometer." In: *Applied optics* (2022). DOI: 10.1364/ao.447762.

[8] Susan Bromley, Larry L. Howell, and Brian D. Jensen. "Determination of maximum allowable strain for polysilicon micro-devices". In: *Engineering Failure Analysis* 6 (1999), pp. 27–41. URL: https://api.semanticscholar.org/CorpusID:137651408.

[9] Timo Veijola. "Chapter 13 - Gas Damping in Vibrating MEMS Structures". In: *Handbook of Silicon Based MEMS Materials and Technologies (Second Edition)*. Ed. by Markku Tilli et al. Boston: William Andrew Publishing, Jan. 1, 2015, pp. 354–373. ISBN: 978-0-323-29965-7. DOI: 10.1016/B978-0-323-29965-7.00013-0. URL: https://www.sciencedirect.com/science/article/pii/B9780323299657000130.

[10] D. Yamane et al. "Design of sub-1g microelectromechanical systems accelerometersa)". In: *Applied Physics Letters* 104.7 (Feb. 18, 2014), p. 074102. ISSN: 0003-6951. DOI: 10.1063/1.4865377. URL: https://doi.org/10.1063/1.4865377 (visited on 05/09/2024).